Supplementary Materials for

Moth resonant mechanics are tuned to wingbeat frequency and energetic demands

Ethan S. Wold[1*], Brett Aiello[4], Manon Harris[2], Usama bin Sikandar[3], James Lynch[5], Nick Gravish[5], Simon Sponberg[1,2]

Corresponding author email address: ethan_wold@gatech.edu

[1]School of Biological Sciences, [2]School of Physics, [3]School of Electrical and Computer Engineering, Georgia Institute of Technology, Atlanta, GA, 30332 USA
[4]School of Natural and Health Sciences, Seton Hill University, Greensburg, PA, 15601 USA
[5]Mechanical and Aerospace Engineering, University of California San Diego, San Diego, CA 92161, USA

This PDF file includes:

Supplementary Text

Stiffness measurements:

After anesthetizing in a refrigerator, moths were prepared for materials testing by removing their wings, legs, head, and abdomen. The metathorax does not deform substantially during flight and likely stores insignificant elastic energy compared to the scutum [1]. Thus, it was removed to fully expose the posterior phragma. Waxy cuticle was gently filed off from the scutum and phragma to support better glue adhesion. Finally, the thoracic ganglion and thoracic musculature were severed to prevent spontaneous muscle contractions from transferring appreciable force to the force sensor.

A custom 3D printed mount was secured to the anterior muscle attachment surface on the scutum with cyanoacrylate glue. The scutum mount was rigidly attached to the drive shaft of an electrodynamic shaker (The Modal Shop 2007E). A #2 threaded rod was glued to the posterior phragma and was screwed into the insert of a piezoelectric force transducer (PCB Piezotronics 209C11). The force transducer was attached to a micromanipulator, giving us precise control over the thorax's rest length. We defined rest length as the length at which no force was measured by the transducer. Importantly, we aligned the thorax such that deformations occurred along the axis that the downstroke muscle would contract in the live animal (Fig. 1a). A fiber-optic displacement sensor (Philtec D47) was used to measure displacement from a strip of reflective tape attached to the shaker drive shaft. The displacement sensor was used only in its linear range and was calibrated daily immediately prior to mounting the first specimen. We prescribed a sine chirp displacement signal from 1-100 Hz at 9% peak-to-peak strain amplitude [2]. The same thorax strain amplitude was used for all species since species-specific strain data could not be analyzed prior to performing stiffness measurements. We do not consider contributions of active muscle stiffness which are relatively small in hawkmoths compared to exoskeletal stiffness [3,4]. Recent work on the thorax of *Manduca sexta* has demonstrated that stiffness and material damping in the thorax are frequency-independent [1,5]. As such, we ignore internal damping in resonance calculations, as it does not affect the location of the resonant peak, and we use the stiffness measured at wingbeat frequency as the thorax stiffness for each species. Our sign convention is such that positive force is generated in the shortening direction.

Muscle strain measurements:

Moths were anaesthetized in a refrigerator, tethered ventrally, and positioned beneath a high-speed video camera (Photron FastCam mini UX100). The moth's abdomen was removed and the middle part of the metathorax was partially dissected away, exposing the posterior phragma, the attachment point for the main downstroke muscles (DLMs). Scales were removed from the anterior scutum, and a white paint pen was used to mark muscle attachment points on each side of the animal. The moth was stimulated to flap by gentle tactile stimulation on the back of its neck. After a flapping bout, the camera was moved to capture wingbeats from the front of the animal, so that wingbeat amplitude could be measured. The order of recording head-on and top-down angles was randomized from individual to individual to ensure moths were not excessively fatigued during a particular filming angle. White markers and wing tips were digitized in DLTdV8 over multiple wingbeats [6]. We define a sign convention such that positive strain is shortening.

In general, we found that tethered moths flapped with wingbeats that were larger in amplitude than those in free-flight [7], likely because of the highly invasive procedure necessary

to expose the posterior phragma and stress due to tethering. To ensure that strain and transmission calculations were not affected by these inflated amplitudes, we computed transmission ratio T directly from the phragma displacement d_{max} and front-view wingstroke amplitude $\phi_{tethered}$ measurements in each moth individually.

$$T = \frac{\phi_{tethered}}{d_{max}} \quad (1)$$

Computing transmission ratio in this way using maximum wingbeat amplitude and maximum strain from the same individual ensure that any inflated wingbeat amplitude is matched by an inflated thorax strain. For a linear and frequency-independent transmission, this will result in an accurate estimation of the transmission ratio. In *Manduca*, we confirmed that the transmission of the wing hinge is linear by recording wingbeats with a time-synchronized two-camera setup (Fig. S1). Plotting wing angle as a function of thorax displacement results in an ellipse, indicating that a linear transmission is likely an appropriate assumption for this group of animals. We defined the operating length L_{op} of the thorax as the mean strain across all digitized wingbeats. We then used T, L_{op} and free-flight wingbeat amplitude ϕ_o to calculate a muscle strain likely to be generated in free-flight by the following equation:

$$\varepsilon = \frac{\phi_o}{TL_{op}} \quad (2)$$

Results of our method for *Manduca* result in a transmission ratio in rough agreement to previous calculations using data from a different study of muscle length changes in a tethered animal [2,3]. For analysis of strain and transmission data, each flight bout from an individual was considered a separate trial. Data was collected from at least three different individuals of each species and was pooled for species-averaged analysis.

Wing inertia and aerodynamic damping calculation:

We leveraged an existing wing morphometric dataset to calculate inertial and aerodynamic parameters for each moth species [8]. Specific imaging and digitization methods are identical to those in Aiello et al. 2021. For *Hyalophora cecropia, Hemaris diffinis, Smerinthus cerisyi, and Sphinx chersis*, we utilized wing shape data from a species in the same genus: *Hyalophora euryalus, Hemaris thetis and Hemaris thysbe, Smerinthus ophthalmica and Smerinthus jamaicensis, and Sphinx kalmiae*. In the above cases, distinctions in wing morphology between species in the same genus were minimal and should not meaningfully affect our results. We compute inertia of the wing pair and added air mass from Eq. 3 [9], where m_w is the mass of the wing pair, R is wing length, $\hat{r}_2(s)$ is the second moment of wing shape, ν is the added mass, and $\hat{r}_2(\nu)$ is the second moment of added mass (see Table S3 for a complete glossary of symbols). In the absence of wing mass distribution measurements across species, we assume, as Weis-Fogh did, that wing thickness is constant, therefore the second moment of mass can be approximated by the second moment of wing area [7,10,11].

$$I = m_w R^2 \hat{r}_2^{\,2}(s) + \nu R^2 \hat{r}_2^{\,2}(\nu) \quad (3)$$

ν was computed from the following equation where $\hat{v}$ is the non-dimensional added mass, ρ is the air density, and A_R is the aspect ratio.

$$\nu = \frac{2\rho\pi\hat{v}R^3}{A_R^2} \quad (4)$$

The parameters in Eq. 3 consider the fore- and hindwings moving together as a combined surface, incorporating inter-clade differences in relative fore- and hindwing area [8]. While lepidopteran flight is primarily driven by the forewing, hindwings play an important role in maneuverability, and may contribute significant mass, especially in silkmoths [12].

We utilized a constant quasi-static aerodynamic damping model with velocity-squared damping, such that the aerodynamic force over a wing stroke is equal to $\Gamma|\dot{\phi}|\dot{\phi}$. This simplified representation of flapping-wing aerodynamics has been used previously to model moth resonant mechanics and its functional form allows for derivation of analytical results that would be impossible with more complex models [3,10,13–15]. The aerodynamic damping parameter Γis computed by the following equation [13], where C_D is the average wing drag coefficient, A_w is the area of the wing pair, and l_{cp} is the non-dimensional location of the center of pressure.

$$\Gamma = \frac{1}{2}\rho C_D A_w \hat{r_2}^2(s) R^3 l_{cp} \quad (5)$$

C_D was computed for each species using eq. 3.2 of Han et al. 2015, averaged over the wing stroke using angle-of-attack data from free-flight kinematics for each species [16]. A constant l_{cp} of 0.6 was used for all species [13], and is widely representative of insect wing centers of pressure across taxa [9].

Calculation of Weis-Fogh number from flight power: The Weis-Fogh number (N) was originally defined as the ratio of peak aerodynamic and inertial torques over a wingstroke [1].

$$N = \frac{\max(\tau_{inertial})}{\max(\tau_{aero})} = \frac{I}{\Gamma\phi_o} \quad (6)$$

While estimates of N using this equation are reasonably accurate when one knows all required information for an insect of interest, it can be challenging to apply Eq. 6 comparatively. Either one must know peak torques from a model (preferably one that incorporates 3D kinematics and/or computational fluid dynamics), or one must know species-specific average drag coefficients and locations of the center of pressure on the wing. Peak torque estimates are not widely reported and wind-tunnel drag coefficient data for many species is not available.

Instead, we use more commonly reported mean cycle-averaged aerodynamic ($\bar{P}_{aero}$) and inertial powers ($\bar{P}_{inertial}$) to compute N. We derive an expression for N that depends on the ratio of these powers using the equation of motion in the main text (main text Eq. 1). Then, we use power estimates for each species from a recent blade-element model that incorporates species-specific wingbeat kinematics to estimate N comparatively.

First, we compute average inertial and aerodynamic power from main text Eq. 1, by integrating the instantaneous power, defined as torque multiplied by angular velocity. Our integration bounds will be the first quarter-stroke (t=0 to t=$\pi/2\omega$), since this is the region during which both aerodynamic and inertial powers are positive. Since we seek the ratio of the mean absolute value of these powers, the result for a quarter stroke will be identical to that for a full stroke and much easier to compute. The inertial power can be written as the following, where $\omega = 2\pi f_{wb}$:

$$\bar{P}_{inertial} = \frac{\pi}{2\omega}\int_0^{\pi/2\omega} I\ddot{\phi}(t)\dot{\phi}(t)dt = \frac{I\phi_o^2\omega^3\pi}{2\omega}\int_0^{\pi/2\omega}\sin(2\omega t)\,dt = \frac{1}{2}I\phi_o^2\omega^2 \quad (7)$$

The aerodynamic power can be written as:

$$\bar{P}_{aero} = \frac{\pi}{2\omega}\int_0^{\pi/2\omega}\Gamma\left|\dot{\phi}(t)\right|\left(\dot{\phi}(t)\right)^2 dt$$
$$= \frac{\Gamma\phi_o^3\omega^3\pi}{2\omega}\int_0^{\pi/2\omega}\cos^2(\omega t)\left|\cos(\omega t)\right| dt = \frac{2}{3}\Gamma\phi_o^3\omega^2 \quad (8)$$

Taking the ratio of Eqs. 7 and 8 and substituting in Eq. 6, we arrive at the final expression for N in terms of $\bar{P}_{inertial}$ and $\bar{P}_{aero}$.

$$N = \frac{4}{3}\frac{\bar{P}_{inertial}}{\bar{P}_{aero}} \quad (9)$$

$\bar{P}_{inertial}$ and $\bar{P}_{aero}$ are then computed for each species using the same model of Aiello et al. 2021 [2]. Aerodynamic power includes contributions from induced, profile, and parasitic power. See the citation and citation supplement for details.

Calculation of aerodynamic efficiency: As discussed in the main text, we derive a new aerodynamic efficiency metric that applies to flapping insects that are not necessarily flapping at resonance. We do this by following the original logic of Weis-Fogh, defining efficiency as the ratio of positive aerodynamic work over a cycle to total positive work (sum of inertial, aerodynamic, and elastic contributions). Following the work of Lynch et al. 2021 [3], we begin with the non-dimensional torques as a function of non-dimensional wing angle:

$$\hat{\tau}_{aero}(t) = 1 - \left(\hat{\phi}(t)\right)^2 \quad (10)$$
$$\hat{\tau}_{inertial}(t) = -N\hat{\phi}(t) \quad (11)$$
$$\hat{\tau}_{elastic}(t) = \hat{K}N\hat{\phi}(t) \quad (12)$$

Aerodynamic efficiency is then defined by the following integral expression, where bounds of integration are chosen to ensure only positive work is being considered.

$$\eta = (100)\frac{\int_+ \hat{\tau}_{aero}(t)d\hat{\phi}}{\int_+ \hat{\tau}_{aero}(t) + \hat{\tau}_{inertial}(t) + \hat{\tau}_{elastic}(t)d\hat{\phi}} \quad (13)$$

From here on, $\hat{\tau}$ and $\hat{\phi}$ are implied to be functions of t for ease of notation. Since $\hat{\tau}_{aero}$ is nonnegative over the domain $\hat{\phi} \in [-1,1]$ we can integrate Eq. 10 directly over this domain:

$$\int_{-1}^{1} \left(1 - \hat{\phi}^2\right) d\hat{\phi} = \frac{4}{3} \quad (14)$$

Note that if $\hat{\tau}_{inertial} = \hat{\tau}_{elastic}$, efficiency is always 100%, which is the case when the insect is flapping at undamped resonance, $\widehat{K} = 1$. So, the denominator integral can be decomposed into two cases: when $\widehat{K} < 1$, and when $\widehat{K} > 1$. In each of these cases, the sum of inertial, elastic, and aerodynamic torques is not positive across the whole domain of integration. We can compute the $\widehat{\boldsymbol{\phi}}$ where the sum of torques crosses zero by finding the zeros of the following two quadratic equations for the $\widehat{\boldsymbol{K}} < \mathbf{1}$ and $\widehat{\boldsymbol{K}} > \mathbf{1}$ conditions respectively:

$$1 - \hat{\phi}^2 + N\left(1 - \widehat{K}\right)\hat{\phi} = 0 \quad (15)$$

$$1 - \hat{\phi}^2 + N\left(\widehat{K} - 1\right)\hat{\phi} = 0 \quad (16)$$

If we call the zeros of these equations $\hat{\phi}^*_{\widehat{K}<1}$ and $\hat{\phi}^*_{\widehat{K}>1}$, we can express the denominator of Eq. 13 piecewise by the following two integrals:

$$\int_{+} \hat{\tau}_{aero}(t) + \hat{\tau}_{inertial}(t) + \hat{\tau}_{elastic}(t) d\hat{\phi} = \begin{pmatrix} \int_{1}^{\hat{\phi}^*_{\widehat{K}<1}} 1 - \hat{\phi}^2 + N\left(1 - \widehat{K}\right)\hat{\phi} d\hat{\phi} & if\ \widehat{K} < 1 \\ \int_{\hat{\phi}^*_{\widehat{K}>1}}^{1} 1 - \hat{\phi}^2 + N\left(\widehat{K} - 1\right)\hat{\phi} d\hat{\phi} & if\ \widehat{K} > 1 \end{pmatrix} \quad (17)$$

Combining the result of Eq. 14 with Eq. 17, one can easily compute η from Eq. 13 with a computer algebra program like Mathematica.

Structural damping impacts on resonance: Dissipation in the hawkmoth thorax has been demonstrated to be frequency-independent, structural damping. We do not consider structural damping in our resonance calculations because it does not meaningfully impact the location of the damped or undamped resonance peak. We demonstrate this in Fig. S3, simulating the displacement and velocity resonance curves for *Manduca sexta*, using a structural damping factor $\gamma = 0.15$ [1,5]. Realistic structural damping changes the resonant frequencies by less than 0.5 Hz, thus it is likely negligible for the current study. We implement the structural damping simulation using the 'equivalent viscous damper' method described in Wold et al. 2023. We also suggest Gau et al. 2019 and Lynch et al. 2021 for more detailed work on the impacts of structural damping for flapping flight.

References:

1. Gau J, Gravish N, Sponberg S. 2019 Indirect actuation reduces flight power requirements in Manduca sexta via elastic energy exchange. *J R Soc Interface* **16**. (doi:10.1098/rsif.2019.0543)
2. Tu MS, Daniel TL. 2004 Cardiac-like behavior of an insect flight muscle. *Journal of Experimental Biology* **207**, 2455–2464. (doi:10.1242/jeb.01039)

3. Gau J, Wold ES, Lynch J, Gravish N, Sponberg S, Sponberg S. 2022 The hawkmoth wingbeat is not at resonance. , 1–5.
4. Tu MS, Daniel TL. 2004 Submaximal power output from the dorsolongitudinal flight muscles of the hawkmoth Manduca sexta. *Journal of Experimental Biology* **207**, 4651–4662. (doi:10.1242/jeb.01321)
5. Wold ES, Lynch J, Gravish N, Sponberg S. 2023 Structural damping renders the hawkmoth exoskeleton mechanically insensitive to non-sinusoidal deformations. *J R Soc Interface* **20**. (doi:10.1098/rsif.2023.0141)
6. Hedrick TL. 2008 Software techniques for two- and three-dimensional kinematic measurements of biological and biomimetic systems. *Bioinspir Biomim* **3**. (doi:10.1088/1748-3182/3/3/034001)
7. Aiello BR, Sikandar U Bin, Minoguchi H, Bhinderwala B, Hamilton CA, Kawahara AY, Sponberg S. 2021 The evolution of two distinct strategies of moth flight. *J R Soc Interface* **18**. (doi:10.1098/rsif.2021.0632)
8. Aiello BR *et al.* 2021 Adaptive shifts underlie the divergence in wing morphology in bombycoid moths. *Proceedings of the Royal Society B: Biological Sciences* **288**. (doi:10.1098/rspb.2021.0677)
9. Ellington CP. 1984 The aerodynamics of hovering insect flight. II. Morphological parameters. *Philosophical Transactions of the Royal Society of London. B, Biological Sciences* **305**, 17–40. (doi:10.1098/rstb.1984.0050)
10. Weis-Fogh T. 1973 Quick estimates of flight fitness in hovering animals, including novel mechanisms for lift production. *Journal of experimental Biology* **59**, 169–230.
11. Pons A, Perl I, Ben-Dov O, Maya R, Beatus T. 2023 Solving the thoracic inverse problem in the fruit fly. *Bioinspir Biomim* **18**. (doi:10.1088/1748-3190/accc23)
12. Jantzen B, Eisner T. 2008 Hindwings are unnecessary for flight but essential for execution of normal evasive flight in Lepidoptera. *Proc Natl Acad Sci U S A* **105**, 16636–16640. (doi:10.1073/pnas.0807223105)
13. Whitney JP, Wood RJ. 2012 Conceptual design of flapping-wing micro air vehicles. *Bioinspir Biomim* **7**. (doi:10.1088/1748-3182/7/3/036001)
14. Lynch J, Gau J, Sponberg S, Gravish N. 2022 Autonomous Actuation of Flapping Wing Robots Inspired by Asynchronous Insect Muscle.
15. Lynch J, Gau J, Sponberg S, Gravish N. 2021 Dimensional analysis of spring-wing systems reveals performance metrics for resonant flapping-wing flight. *J R Soc Interface* **18**. (doi:10.1098/rsif.2020.0888)
16. Han JS, Kim JK, Chang JW, Han JH. 2015 An improved quasi-steady aerodynamic model for insect wings that considers movement of the center of pressure. *Bioinspir Biomim* **10**. (doi:10.1088/1748-3190/10/4/046014)

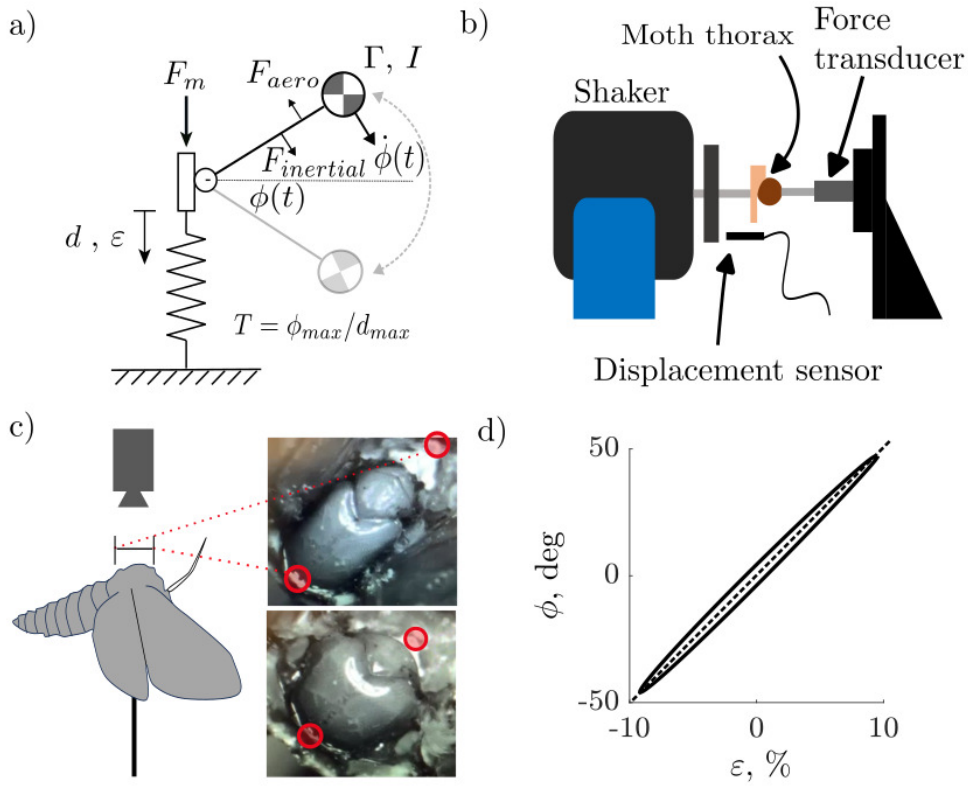

Figure S1: Measurement of spring-wing thorax parameters. a). Free-body diagram of generalized spring-wing model showing the geometry of the actuating muscles, thoracic spring, transmission, and inertial wing. b). Schematic of the experimental apparatus used to measure thorax stiffness, consisting of an electrodynamic shaker, fiber-optic displacement sensor, and piezoelectric force transducer. c). Schematic of a moth filmed from above on a tether, with inset photographs showing the DLM attachment points at maximum and minimum strain. d). Average wing stroke angle as a function of thorax strain in one representative *Manduca* individual. The transmission ratio (slope of the ellipse denoted by dashed line) does not deviate substantially from linearity over a wing stroke.

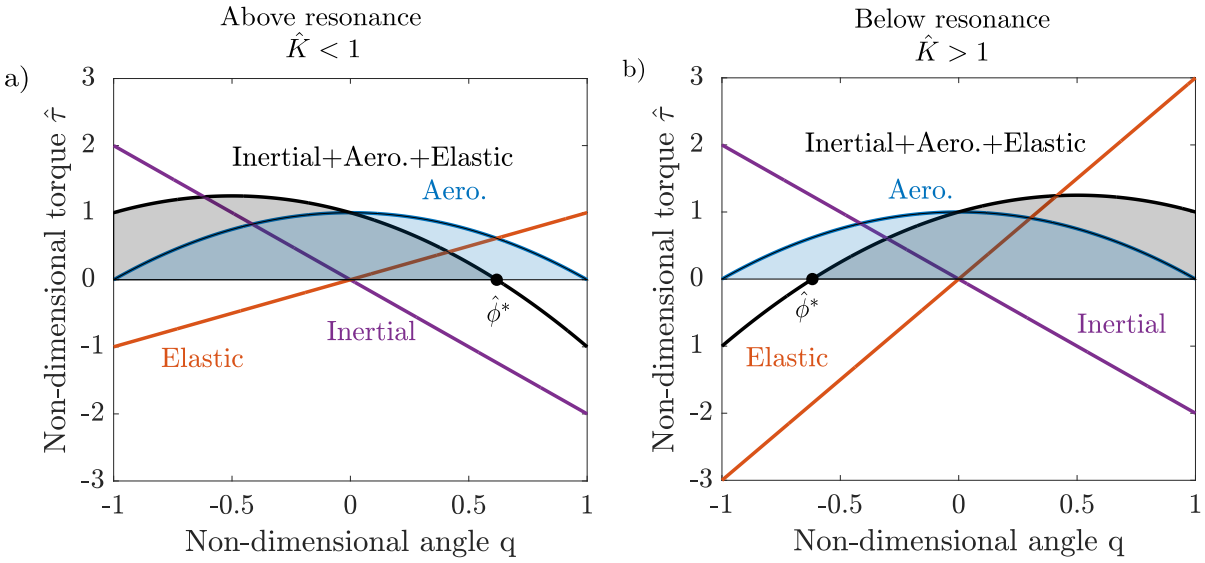

Figure S2: Aerodynamic efficiency above and below resonance. A). Non-dimensional torques as a function of wing angle in the above-resonance case, with the integration bound $\hat{\phi}^*$ notated. **B).** Non-dimensional torques as a function of wing angle in the below-resonance case, with the integration bound $\hat{\phi}^*$ notated. Shaded blue and black areas correspond to aerodynamic work and total positive work respectively.

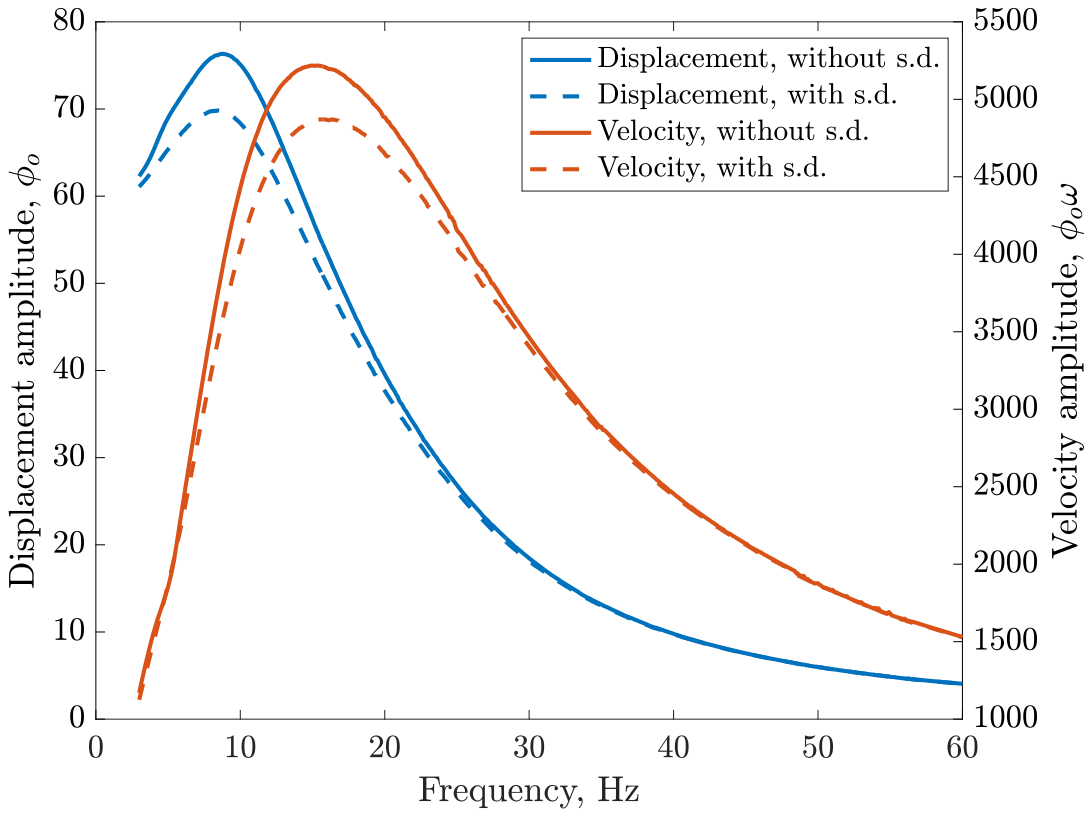

Figure S3: Effects of internal damping on resonance. Simulated displacement and velocity resonance curves for *Manduca sexta,* with and without structural damping (s.d.). A representative structural damping factor of 0.15 was used in simulation.

Species	$\hat{r}_2(s)$	m_w (g, both wings)	R (m)	$\hat{r}_2(v)$	A_R, both wings	$\hat{v}$	A_w (m^2, both wings)	C_D	f_{wb}, Hz	$2\phi_o$, deg
Automeris io	0.506	0.0452	0.0326	0.4712	3.1854	1.18	0.001346	0.4	22	129
Hyalophora cecropia	0.492	0.1322	0.0596	0.4373	3.5178	1.17	0.00406	1.3	13	110
Smerinthus cerisyi	0.504	0.0354	0.0366	0.4586	4.9164	1.12	0.001128	1.2	33	105
Sphinx chersis	0.516	0.0436	0.045	0.4783	6.5784	1.08	0.001252	1.1	31	88
Hemaris diffinis	0.524	0.0084	0.0199	0.4898	6.6964	1.08	0.000248	2.6	62	91
Hyles lineata	0.497	0.0328	0.0374	0.4448	5.7654	1.1	0.000974	1.5	35	117
Actias luna	0.486	0.1172	0.0518	0.4296	3.2842	1.2	0.00331	0.4	14	130
Manduca sexta	0.53	0.061	0.0528	0.482	6.637	1.08	0.001678	1.5	25	117
Antheraea polyphemus	0.502	0.162	0.066	0.4537	4.1396	1.18	0.004232	0.7	10	134
Citheronia regalis	0.484	0.125	0.0612	0.4376	3.8138	1.17	0.0028	0.6	15	132

Table S1. Wing shape parameters. All data necessary to compute inertia and aerodynamic damping parameter for each species, as well as free-flight wingbeat frequency and free-flight peak-to-peak wingbeat amplitude. Unitless quantities unless otherwise specified.

Quantity	Dimensions	Slope	r^2	p-value	PGLS slope	PGLS r^2	PGLS p-value
$\sqrt{k}$	$N^{0.5}m^{-0.5}$	0.003	<0.01	0.971	-0.054	0.037	0.595
ε	%	-0.338	0.624	0.007*	-0.338	0.624	0.007*
T	rad m^{-1}	63.723	0.850	<0.001*	67.852	0.836	<0.001*
$\log_{10}(I)$	kg m^2	-0.047	0.925	<0.001*	-0.047	0.925	<0.001*
k_{rot}	Nm rad^{-2}	-2.299e-5	0.442	0.036*	-2.299e-5	0.442	0.036*
$\widehat{K}$	Unitless	-0.009	0.240	0.151	-0.009	0.240	0.151
f_{nat}	Hz	0.607	0.890	<0.001*	0.701	0.887	<0.001*
f_{res}	Hz	0.417	0.629	0.006*	0.418	0.635	0.006*

Table S2: Regression statistics. Regression and PGLS slopes and r^2 values for each quantity in main text Figs. 3-5 plotted against wingbeat frequency.

Symbol	Quantity	Dimensions
A_R	Aspect ratio (both wing pairs)	Unitless
A_w	Wing area (both wing pairs)	m^2
C_D	Average drag coefficient	Unitless
d_{max}	Maximum thorax displacement	m
F	Muscle force amplitude	N
f_{nat}	Natural frequency	Hz
f_{res}	Resonance frequency	Hz
f_{wb}	Wingbeat frequency	Hz
I	Wing inertia	kg m^2
$\widehat{K}$	Inertial power offset	Unitless
k	Thorax stiffness	N/m
l_{cp}	Location of center-of-pressure	Unitless
m_w	Wing mass (both wing pairs)	kg
N	Weis-Fogh Number	Unitless
$\bar{P}_{acc}$	Wingstroke-averaged inertial power	W
$\bar{P}_{aero}$	Wingstroke-averaged aerodynamic power	W
R	Wing length	m
$\hat{r}_2(s)$	Second moment of wing shape	Unitless
$\hat{r}_2(v)$	Second moment of added mass	Unitless
T	Transmission ratio	rad/m
Γ	Aerodynamic damping parameter	kg rad m^2
ε	Thorax strain	Unitless
η	Aerodynamic efficiency	Unitless
v	Added mass	kg
$\hat{v}$	Nondimensional added mass	Unitless
ρ	Air density	kg/m^3
ϕ_o	Free-flight wingbeat amplitude	rad
$\phi_{tethered}$	Tethered wingbeat amplitude	rad
$\hat{\phi}$	Nondimensional wing angle	Unitless
$\hat{\tau}_{aero}$	Nondimensional aerodynamic torque	Unitless
$\hat{\tau}_{inertial}$	Nondimensional inertial torque	Unitless
$\hat{\tau}_{elastic}$	Nondimensional elastic torque	Unitless

Table S3: Symbol glossary